AlGaN/GaN HEMTs with very thin buffer on Si (111) for nanosystems applications

2014 Semicond. Sci. Technol. 29 115018

(http://iopscience.iop.org/0268-1242/29/11/115018)

Semicond. Sci. Technol. **29** (2014) 115018 (9pp)

doi:10.1088/0268-1242/29/11/115018

AlGaN/GaN HEMTs with very thin buffer on Si (111) for nanosystems applications

P Leclaire[1,2], S Chenot[1], L Buchaillot[2], Y Cordier[1], D Théron[2] and M Faucher[2]

[1] UPR10 CRHEA-CNRS, rue Bernard Grégory, 06560 Valbonne, France
[2] IEMN, CNRS UMR 8520, Avenue Poincaré, BP60069, 59652 Villeneuve d'Ascq Cedex, France

E-mail: ple@crhea.cnrs.fr

Received 29 April 2014, revised 6 August 2014
Accepted for publication 27 August 2014
Published 26 September 2014

Abstract

In the present work, AlGaN/GaN high electron mobility transistors (HEMTs) have been grown with very thin buffer layers on silicon substrates in view of developing nano electromechanical systems (NEMS) for sensors applications. To ensure transducer operation in the MHz range together with low mechanical stiffness, epitaxial structures with thickness below 1 μm have to be developed. We report on the evolution of the material and electrical properties of AlGaN/GaN HEMTs with thicknesses varying from 2 μm to 0.5 μm. The set of parameters obtained includes in-plane Young modulus of 250 GPa in association with carrier density of 6×10^{12} cm^{-2} and mobility above 1000 cm^2 V^{-1} s^{-1}. The resulting behavior of demonstration transistors validates these epilayers for electromechanical resonators operation.

Keywords: GaN, HEMT, MEMS

(Some figures may appear in colour only in the online journal)

1. Introduction

Micro-electro-mechanical systems (MEMS) are widely investigated for their applications in actuators and sensors. In the area of vibrating resonant devices, most are based on silicon technology. Even if Si based resonators exhibit ultrasensitive mass/force detection [1–4] they lose their mechanical [5] and electrical properties for temperature higher than 200 °C. Therefore, their use in harsh environments is difficult. To overcome these intrinsic limitations, other approaches such as wide bandgap semiconductor have been investigated. Among those materials, III-nitrides and SiC [6–10] emerge for their mechanical properties [11–14] as well as their thermal stability [15–17]. The easy integration, high efficiency and low power consumption of piezoelectric actuators appear as particularly advantageous [18] compared to the electrothermal [19] or electrostatic [20] ones. As SiC has low piezoelectric constants, group III nitrides seems to be more adapted to achieve resonant devices with piezoelectric transducer. In particular, GaN is able to withstand high electric fields and remains piezoelectric at high temperatures [21–23]. Furthermore, Group III-nitride semiconductor devices and especially AlGaN/GaN high electron mobility transistors (HEMTs) are now established as leading components for power switching and RF communications [24–27]. These purely electronic applications have driven material improvements, but devices that combine MEMS and electron transport are currently emerging on GaN basis [28–31]. In a previous work we have shown that the piezoelectric properties combined to the two-dimensional electron gas (2DEG) can be used to achieve resonators [29, 32]. Using transducers based on AlGaN/GaN HEMT structure, a fundamental resonance frequency of 4 MHz has been obtained for device dimensions of $(L \times W \times T) = 2\,\mu\text{m} \times 5\,\mu\text{m} \times 20\,\mu\text{m}$ [33]. L, W and T are the beam length, width and thickness, respectively.

To address a large range of applications from mass sensing to RF filter, the development of ultra-sensitive devices with very high bandwidth [34, 35] is needed. To achieve such devices, two challenges have to be addressed in parallel: 1) increasing the device frequency [36], and 2) keeping low stiffness [37–39]. Furthermore, to maintain an efficient transducer coupling to the flexural mode the device aspect ratio has to be preserved. In order to reach UHF range ($f > 100$ MHz), all dimensions must be downscaled [40, 41]. For a GaN resonator working in UHF, typical relevant dimensions would have to be ($L \times W \times T$) = 0.5 μm × 1 μm × 5 μm.

In the known epitaxial structures developed for high frequency/high power electronic applications, thick GaN buffer is used to reduce the effect of the parasitic capacitance with the silicon substrate and to withstand high voltages [42–44]. Because of the large mismatch of lattice parameters and thermal expansion coefficients (TEC) between GaN and Si [45], more than 1 μm thick GaN buffer layers have to be grown on about 0.5 μm thick AlN/GaN [29] or AlN/AlGaN stress mitigating stacks. More recently, a 100 nm thick HEMTs structure with an electron mobility as high as 1100 $cm^2 \cdot V^{-1} \cdot s^{-1}$ has been reported on Al_2O_3 substrate [46], but microsystem technology with released structures needs GaN on silicon. For NEMS transducers operation, downscaled buffers have to be optimized in order to limit the devices degradations. Indeed, an efficient resonator actuation requires reduced electrical leakages and the motion detection (connected to the transistor transconductance) [32] requires an acceptable 2DEG conductivity with an electron mobility $\mu > 500\ cm^2\ V^{-1}\ s^{-1}$ and a carrier density $Ns > 5 \times 10^{12}\ cm^{-2}$ typically. Furthermore, in order to reduce noise-to-signal ratio in future systems, keeping a transistor with acceptable performances in the vicinity of the resonator is highly desired.

Here we study the effect of buffer stack and thickness on electrical properties of AlGaN/GaN HEMT structures on Si (111). Three approaches to downscale the buffer have been investigated by x-ray diffraction, transmission electron microscopy (TEM) and Hall measurement. For structures from 1 μm to 500 nm thick, 2DEG carrier density and mobility that exceed $5 \times 10^{12}\ cm^{-2}$ and 1000 $cm^2\ V^{-1}\ s^{-1}$ have been obtained. Finally, DC *I–V* characteristics and breakdown voltage measurements of HEMTs devices are analyzed.

2. Experimental

AlGaN/GaN HEMT structures were grown by molecular beam epitaxy (MBE) on high resistivity Si (111) substrates ($\rho > 5\ k\Omega$ cm) in a Riber Compact 21T reactor using ammonia as nitrogen source [47]. Prior to the growth, substrates were cleaned by means of a 2.5% diluted HF solution for 2 min A 100–200 nm AlN seed layer was grown at 920 °C on each sample. Growth conditions and layer stacking have to be chosen in order to avoid layer cracking due to the ~1GPa TEC mismatch related tensile stress induced upon cooling down to room temperature. Moreover, after releasing the final device, buckling effect has to be avoided, meaning that the large strain gradient present in our previously developed thick structures [48] is not suitable. Then, the buffer structures were progressively modified in order to reach a 500 nm thick structure. From a 2.4 μm thick structure with an AlN interlayer we have reduced the total structure thickness down to 0.52 μm (table 1). HEMT structures composed of a 3 nm GaN cap layer, a 21 nm AlGaN barrier with a 28% (+/−1%) Al content, as determined by x-ray diffraction (XRD) and a 1 nm AlN spacer were grown on the GaN-on-Si buffers. Sample quality and morphology were assessed by XRD and tapping mode atomic force microscopy (AFM), respectively. Cross sectional transmission electron microscopy (TEM) was performed using a JEOL 2010F equipment. Threading dislocation density counting was carried out by AFM after annealing under NH_3 environment [49].

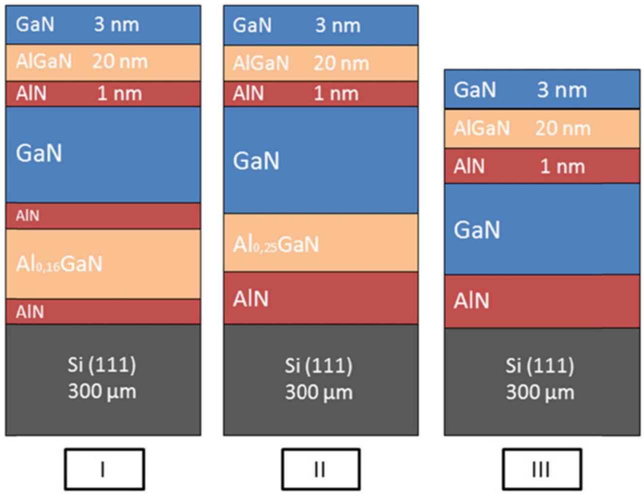

Figure 1. Schematic representation on the three types of structures that have been studied for reducing the buffer thickness: buffer with AlN and AlGaN interlayers (I), buffer with AlGaN intermediate layer (II) and thin buffer on AlN seed layer (III).

A photolithographic process was applied to make test devices such as van der Pauw, isolation patterns, transfer length method (TLM), circular diodes and transistors. The process starts with mesa isolation by etching the active layers with $Cl_2/CH_4/Ar$ plasma in a reactive ion etching (RIE) reactor. After a partial etching of the AlGaN barrier, Ti/Al/Ni/Au ohmic contacts were deposited by e-beam evaporation and annealed at 740 °C for 30 s under N_2 environment. Ni/Au gate of 4 μm length and 150 μm width were deposited for making transistors with a drain-to-source distance of 16 μm. Finally, Ni/Au access pads were deposited. DC *I–V* characterizations of TLM, diodes and transistors were performed using Keithley 2400 source meters.

3. Results and discussion

3.1. Material characterizations

In order to find the best stack for reducing the thickness while keeping good crystal properties, a study of GaN buffer quality of several structures with different thicknesses has been done. Figure 1 shows the different buffer stacks we grew for this study. Here we distinguish 3 types of buffer: buffer with AlN and AlGaN interlayers (I) inspired by the typical RF/power HEMT structure, buffer with AlGaN intermediate layer (II) and buffer without interlayer (III).

The full width at half of maximum (FWHM) of the (302) and the (002) GaN omega scan XRD peak have been measured for the films grown following the different approaches (table 1, figure 2). Such a width is proportional to the threading dislocation density (TDD) [50]. However, the (002)

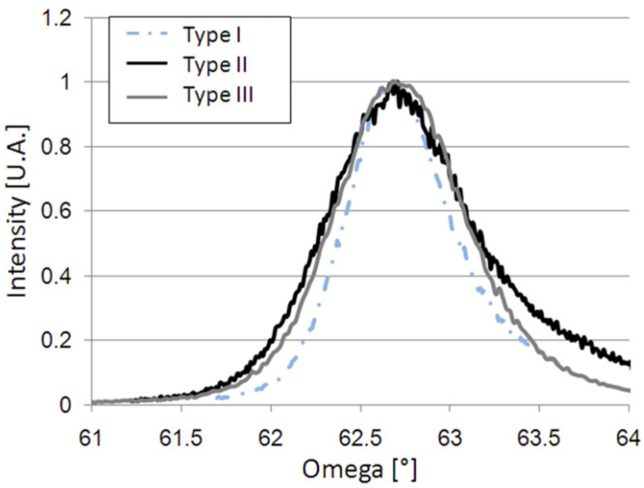

Figure 2. GaN (302) omega scans for the 3 buffer types with a 500 nm thick GaN buffer.

omega scan FWHM is more sensitive to screw type (named as c dislocations) threading dislocations and to the bent mixed type (a + c) dislocations (including dislocation loops), whereas the (302) FWHM accounts for all types of threading dislocations. Figure 3 shows the FWHM of the (302) GaN as a function of the buffer type and thickness. Due to the more grazing incidence of the x-ray beam in this configuration, the width is expected to be more sensitive to the quality of the surface layers. However, as the probed thickness is estimated to about 500 nm, measurements performed on the thin structures give only an average picture of the crystal quality of the GaN layer. As shown here for type I and type III structures, a common trend is the defect density reduction with the thickening. Now focusing on 1 μm thick structures, the type II structures with an $Al_{(x)}Ga_{(1-x)}N$ ($x_{Al} = 25\%$) intermediate layer between the AlN seed layer (nucleation layer) and the GaN buffer exhibit noticeably larger FWHM values.

In type I structures, the reduction of the interlayers thicknesses (table 1) leads to FWHM around 3000 arcsec which is almost equivalent to those obtained for structures without interlayers (type III). This is due to the poor dislocation filtering capability of thin interlayers since each layer thickness is not thick enough to completely relax its stress. Indeed, the lattice mismatch strain/stress is a driving force for dislocation bending and annihilation. The best quality type I structure has been obtained for AlN and AlGaN interlayers of about 100 nm and 200 nm, respectively. From this point and due to the slow strain relaxation rate in the GaN buffer in type I structure, achieving a 500 nm thick structure showing fully relaxed layers, and especially the GaN buffer, is really difficult.

Furthermore, the difference in crystal quality between type I and III structures tends to be less and less significant as the total thickness is reduced. Thus, for crystal quality, the advantage of using interlayers or intermediate layers vanishes compared to the complexity of growing such structures when reaching submicron thicknesses. Finally, type III scheme seems to be the best way to reduce the thickness since such samples exhibit good crystal quality while using a simpler growth process. Moreover, as our structures have total thicknesses well below 1 μm, the structures are no longer subject to a risk of cracking in spite of the large TEC mismatch induced stress.

Figure 4 shows a cross sectional TEM image of a type III sample with a 300 nm GaN buffer on a 200 nm AlN seed layer. One notes the large density of threading defects in the AlN layer, followed by a transition region with bent dislocations as well as dislocation loops (vertical arrow) and finally a reduced number of more or less inclined threading dislocations (horizontal arrows) reaching the surface. The presence of dislocation loops indicates that a fast relaxation of the 2.5% compressive mismatch strain between GaN and AlN takes place in the bottom transition region of the GaN film (vertical arrow in figure 4).

Considering the initial number of defects in the AlN seed layer ($>10^{11}$ cm^{-2}) it is obvious that the loop formation process is quite efficient for dislocation filtering. On the other hand, most of the inclined dislocations threading into the rest of the GaN layer have Burgers vector with an in-plane edge component (a, a + c) and participate to a slow strain relaxation and defect filtering process.

Previously, we have observed that the dislocation bending angle is sensitive to the residual compressive strain during the growth [48] as well as to the growth conditions [51]. The observed bending points out that the top region of the GaN layer is not fully strain relaxed and slow dislocation filtering will continue within thicker GaN layers. Thus, the growth of a 300 nm GaN layer seems to be a lower limit to obtain fully relaxed GaN buffer layer in the present type of structure.

We have calculated the in-plane strain from XRD lattice parameter measurements and compared with FWMH of the GaN (302) XRD peaks (table 1). The general trend is an enhancement of the crystal quality with the reduction of the residual tensile strain. To explain this result, we have to consider two effects. First, the strain relaxation is promoted by the dislocation bending which allows interactions and loop formation. A high TDD at the growth front will thus enhance the strain relaxation mechanisms. In terms of average strain, a large relaxation rate will lead to a high tensile stress upon cooling down from the growth temperature (800 °C) down to room temperature. Second, a fast strain relaxation regime takes place in the bottom region of the GaN film. In this region (vertical arrow in figure 4), the 2.5% compressive mismatch strain between GaN and AlN is rapidly relaxed and generates dislocation loops. Even though this fast relaxation process is efficient for dislocation filtering, it can reduce the strain at a level sufficiently low to drastically slow and sometimes to inhibit further dislocation bending, interactions and filtering [48]. So, there is a trade-off between strain relaxation and dislocation filtering efficiency. This scenario is confirmed in our samples since the strain relaxation rate is larger for structures with the highest TDD. From these observations we can say that the use of AlN and AlGaN interlayers (type I) efficiently reduces the residual tensile strain in the GaN buffer compared to types II and III.

Table 1. Material characteristics of the studied buffers with various stacks and thicknesses. The highlighted lines are for structures used for electrical characterizations.

Buffer structure	Total Thickness [μm]	GaN buffer thickness [nm]	RMS [nm]	FWHM (002) [Arcsec]	FWHM (302) [Arcsec]	In plane strain εxx [%]	TDD [cm^{-2}]
Type I: GaN buffer with AlN and AlGaN interlayers	2.422	1730	4.2	756.5	1728		
	1.05	500	1.9	1252.8	2311	0.10	$9*10^9$
	0.815	600	1.7	972	3168		
	0.715	620	1.8	1008	2808		
	0.726	360	2.5	939.6	2206.8	−0.26	
Type II: GaN buffer with AlGaN interlayer	0.985	500	3.2	975.6	3088	0.31	
	1.05	500	2.5	1011.6	3290	0.24	
Type III: GaN buffer on 200 nm AlN seed layer	2	1800	2.8	752.4	2880		
	1.95	1800	2.2	666	2275		
	0.825	600	1.3	936	2772		
	0.725	500	1.4	990	3024	0.16	$1.7*10^{10}$
	0.525	300	0.84	1252.8	3391	0.61	$3.5*10^{10}$

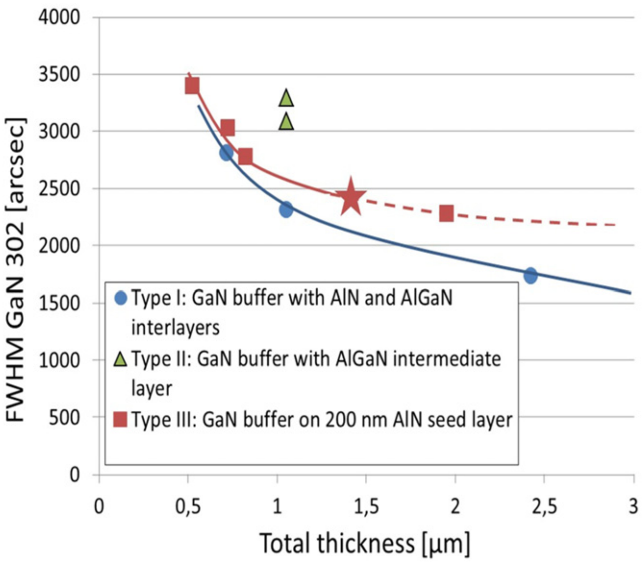

Figure 3. Evolution of the GaN buffer quality determined by XRD, as a function of the total thickness for the three used stack. Red star shows the thickness beyond which we observe cracks.

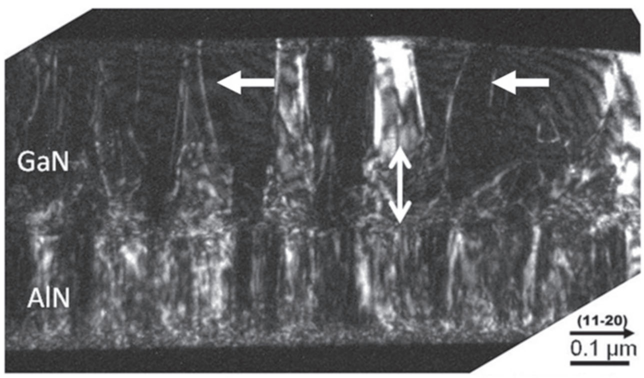

Figure 4. Dark field TEM image of 300 nm GaN on 200 nm AlN seed layer. The image was taken along the [11–20] direction and contains a and a + c dislocations type. Horizontal arrows indicate bent dislocations, and the vertical one the strain relaxation zone in GaN.

For NEMS applications, a residual tensile stress is preferable to avoid buckling when releasing doubly clamped beams or membranes. Thus, growth parameters as well as used stacks have to be chosen to obtain crack-free structures in spite of the tensile stress. However, due to the lower strain relaxation rate it is harder to fulfill this criterion on thin structure using type I, which is used to achieve thick crack-free GaN buffer, and makes it more sensitive to buckling effect. Indeed, by using the optimized interlayer stack to increase the crystal quality while keeping a low thickness (0.760 nm), the structure shows a compressive residual stress of −0.26% (table 1). Nevertheless, a solution to avoid buckling effect in a thin type I structure may be to accelerate the strain relaxation via a 3D growth mode like the one induced by interface treatment such as SiN [52]. In view of reducing the structure thickness while keeping a reasonable defect density and a mean tensile strain, the type III structure seems to be, at this step, the best one for NEMS applications.

Lastly, nanoidentation has been performed on type I and type III samples using a Berkovich diamond indenter previously calibrated on a SiO_2 sample. In- plane Young modulus of four samples with total thicknesses from 1.4 μm to 0.7 μm has been carried out along with a 5 μm GaN-on-sapphire template (TDD ~ 3×10^8 cm^{-2}) that we use as a reference. To limit the substrate contribution on the elastic response of the epitaxial layer, the indenter maximum vertical displacement has been set to 200 nm. This value provides the best tradeoff between small depth and measurements reproducibility.

Figure 5 shows the Young modulus values as a function of the FWHM of the GaN XRD peaks. One can note the 17% drop compared to the 5 μm thick reference which could be attributed to either the lower crystal quality or the parasitic elastic response of the substrate. About the thin buffers, the variation of Young modulus appears as quite limited despite the large range of FWHM. However, we notice a weak decrease of the Young modulus with the increase of the GaN (002) FWHM when no trend is observed with the (302) FWHM widening. Furthermore, Type I exhibit a lower

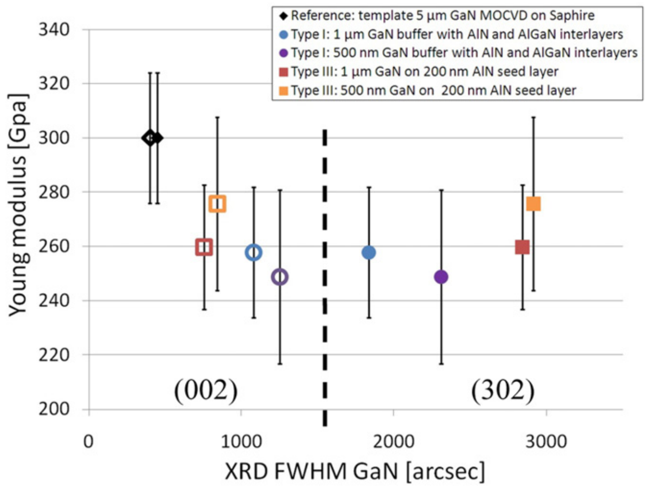

Figure 5. Young modulus measured on Type I and Type III structures as a function of the XRD FWHM of the GaN buffer. Filled symbols are used for GaN (302) reflexion and open symbols for the GaN (002) one.

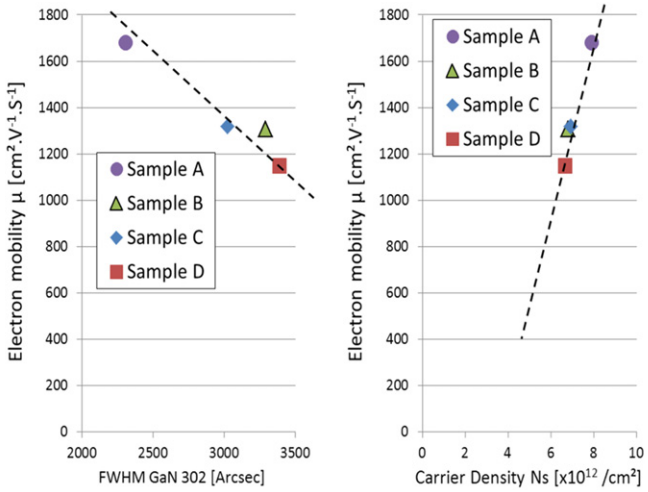

Figure 6. Electron mobility against (left) GaN (302) FWHM and (right) carrier density for processed samples. The dotted line is a guide for the eye.

Young modulus than type III. Several phenomena might induce such behaviors. First, the presence of buried cracks on type I structures [53] might be responsible for lower Young modulus measurement results. Second, the (002) omega scan is more sensitive to screw type threading dislocations and bent edge dislocations, whereas the (302) is affected by all kind of dislocations [50]. Since type I exhibit a larger (002) FWHM, screw dislocations or dislocations with in-plane component might therefore have an effect on the Young modulus measurement results.

With the view of fabricating NEMS devices, the 17% drop of the in-plane Young modulus is acceptable. Indeed, according to Euler–Bernoulli equation [41], it will result in a 0.9% decrease on the resonant frequency which will be balanced by the buffer thinning. Elastic properties measured on thin film confirm that type III is the most suitable structure for NEMS applications. Let us now investigate the electrical properties of these structures and their device behavior.

3.2. Electrical properties

Table 2 shows the electrical properties of the 2DEGs in HEMTs achieved on the previously presented buffers and referenced here as samples A, B, C and D. Sample A is of type I, sample B is of type II and samples C and D are of type III. Here we focus on structures with already downscaled buffer designed for NEMS operating at 100 MHz. Thus, we will only discuss structures with buffer thicknesses of 1 μm or less. From the thinning of an HEMT structure inspired from RF/power (sample A) to a structure optimized for NEMS application (sample D), the electron mobility and carrier density are reduced by 32% and 15%, respectively. However, since our device operates at 100 MHz, this 2DEG properties degradation is still acceptable.

Figure 6 shows the electron mobility, measured by Hall effect, against the FWHM of the GaN (302) XRD peak. The linear increase of the mobility with the reduction of the FWHM as well as the linear trend of the mobility against the carrier density indicates that the main scattering effect involves the charged dislocations [54]. Lastly, a concomitant decrease of the 2DEG carrier density Ns while reducing the thickness leads to the increase of the sheet resistance *R*sh. This is also related to an increase of the threading dislocation density [55]. In summary, as we could have expected, the 2DEG transport properties are strongly dependent on the TDD and so on the buffer thickness. Despite the high dislocation density, the mobility of 2DEG is still superior to 1100 $\mathrm{cm^2\,V^{-1}\,s^{-1}}$, even for total thicknesses reduced down to 0.5 μm.

3.3. HEMT characterizations

For NEMS applications three aspects of HEMT devices have to be investigated: 1) their properties in the linear regime (in particular the transconductance gm) necessary for transducer operations [29, 32, 33], 2) the I_{on}/I_{off} drain current ratio and the breakdown voltage necessary for integrating electronic functions on the same wafer, and 3) the gate leakage current to be lowered for an optimized actuation. *I–V* measurements were carried out on transistors with a 4 μm × 150 μm gate at the center of source to drain spacing of 16 μm. All the devices exhibit an *I–V* characteristic with flat saturation and good pinch-off. Their main characteristics extracted from DC *I–V* measurements are reported in table 3. In this table are shown the properties of a similar transistor fabricated on a 2.2 μm thick HEMT structure developed for RF applications [43].

Figure 7 shows the common source DC output characteristics of transistors on samples C and D for a gate bias *Vgs* varying from 0 to −4 V with a −1 V step. Focusing on the thinnest type III structures, we can see that samples C (730 nm) and D (530 nm) exhibit a drain current of 232 and 209 mA $\mathrm{mm^{-1}}$ at *Vgs* = 0 V, respectively, which is about half of the current measured on sample A (not shown) while the contact resistance *Rc* is 0.5 Ω mm (0.4 Ω mm for sample A). Although the drain leakage current in sample D is almost 30

Table 2. Electrical properties, measured by Hall Effect at room temperature, of AlGaN/GaN HEMT on 4 different buffers.

Buffer structure	Ns [10^{12} cm^{-2}]	μ [cm^2 V^{-1} s^{-1}]	Rsh [Ω/□]
Type I: 500 nm GaN buffer with AlN and AlGaN interlayers (Sample A)	7,96	1680	467
Type II: 500 nm GaN buffer with AlGaN interlayer (Sample B)	6,82	1306	701
Type III: 500 nm GaN buffer on 200 nm AlN seed layer (Sample C)	6,96	1319	680
Type III: 300 nm GaN buffer on 200nm AlN seed layer (Sample D)	6,72	1147	810

times larger than in sample C, the I_{on}/I_{off} drain current ratio is still superior to 2×10^3 while the transconductance (gm) is reduced by 10% only. On the other hand, despite better 2DEG properties, sample A is limited by its high gate leakage current which explains the poorer I_{on}/I_{off} ratio of 4×10^2.

As shown in figure 7, the structures exhibit a good gate control with a pinch-off voltage around −4 V. Except for sample A, I_{on}/I_{off} drain current ratio higher than 10^3 is observed up to the drain bias Vds = 8 V. The monotonous evolution of the maximum drain current Ids and the pinch-off voltage Vp (table 3) with the 2DEG sheet resistance confirms the normal operation of the transistors.

In our devices, transducers are based on piezoelectric effect that takes place in the barrier when an electric field is applied between the gate and the 2DEG. It has been showed that NEMS piezoelectric actuation is more efficient when the HEMT exhibits low gate leakage and high breakdown field [32]. On one hand, HEMTs were biased at Vgs = −7 V and a sweep from 0 to 200 V was applied to the drain bias in order to measure the drain and gate leakage currents with a compliance of 1 mA mm^{-1} (figure 8). On the other hand I–V measurements were performed on 100 μm width isolation patterns with a 20 μm gap (buffer resistivity table 3) and circular diodes (figure 9).

As shown in figure 8, different behaviors are observed. First, transistors on samples A and D present a poor breakdown voltage, 17 V and 18 V, respectively. In the case of sample A, the breakdown voltage is strongly impacted by the low buffer resistivity (<105 Ω mm) as reported in table 3, and by the large gate leakage current (figure 8—right and figure 9). In type I structures, the noticeable degradation of the buffer resistivity and the electrical strength while reducing the GaN thickness has been previously observed [56]. One possible origin of the leakage in this type of structure may be the combination of two effects, more or less significant depending on the thickness of each layer: 1) the different dislocations arrangements and densities which vary in the depth of structure, and 2) the distribution of the impurities (especially silicon, oxygen and carbon) with concentrations dropping from the bottom of the AlN nucleation layer and stabilizing by steps in the following layers [57]. Lastly, the electrical properties of the interlayers in the presence of buried cracks [53] are not well known.

On the other hand, transistors on sample D exhibit a low breakdown voltage (figure 8), but the buffer resistivity is high (~3×10^6 Ω mm). Both the drain leakage and the gate leakage of the transistors follow the same trend but the reverse gate leakage current measured on circular diodes is very low (figure 9). This difference is due to the fact that, in our mask set, the gate contact pad in transistors is deposited on the GaN buffer, whereas the Schottky contact of circular diode is deposited on the GaN cap. Thus, the main part of the leakage current measured on transistor D comes from charges that flow through the buffer while the gate leakage is as low as in sample C.

Moreover, samples B (type II) and C (type III) exhibit a saturation of the leakage current beyond 30–40 V (red circle in figure 8). This behavior is attributed to the different resistivity and electrical strength of each layer as well as the density of traps located in the buffer [58]. As for sample D, the transistor drain leakage current is linked to the gate leakage via the gate contact pad. Compared to sample C (breakdown voltage of 90 V), the insertion of a thick AlGaN intermediate layer, in sample B seems to be an efficient way to increase the breakdown voltage to more than 200 V (limit of our apparatus), but at the expense of an increase of the total thickness. In contrast, I–V measurements on circular diodes on type III structure (samples C and D) exhibit a lower reverse gate leakage current than type II sample B (figure 9). According to the literature [54, 59], this difference could be attributed to the type of TDs that threads into the AlGaN barrier. In our case, a larger leakage current in type II structure may be related to a higher screw type threading dislocations density than in type III. FWHM of GaN (002) (table 1) confirms this hypothesis. These opposite behaviors show a competition between the breakdown voltage enhancement and the gate leakage reduction in thin films. Moreover, it points out that the electrical behavior of TDs in the barrier changes with the layers stack underneath. However, for the targeted application, the use of MOS-HEMT or MIS-HEMT structure could significantly mitigate the gate leakage in the type II structure.

Lastly, as samples C and D are both type III and differ only by the GaN layer thickness (500 nm and 300 nm, respectively) which results in a decrease of the breakdown voltage from 94 V to 18 V, one can conclude on the critical properties of the first hundreds nanometers of GaN grown on the 200 nm AlN seed layer in this type of structure. However, the critical increase of the gate leakage is only visible when a bias is applied to the drain. As shown in figure 9, the diode reverse gate leakage currents of sample C and D are almost the same (<0,06 A cm^{-2}) which presumes a similar dislocation type and density. Thus, a trade-off between AlGaN interlayer and GaN buffer on AlN seed layer has to be found to increase the breakdown voltage (if required) while keeping good HEMT performances and low thickness.

Table 3. Main DC characteristics of transistors on type I, II and III HEMT structures.

Sample	Total Thickness [μm]	GaN buffer thickness [nm]	Ids [mA mm^{-1}]	gm [mS mm^{-1}]	Vp [V]	I_{on}/I_{off} ratio	Buffer resistivity (8V) [Ω mm]	Vbr [V]
Type I [43]	2.167	1730	712	155	–4.9	Na	Na	Na
Sample A (type I)	1.05	500	430	114	–4.4	4.0×10^{2}	3.3×10^{4}	17
Sample B (type II)	1.05	500	219	94	–4.32	5.2×10^{4}	2.5×10^{4}	>200
Sample C (type III)	0.725	500	230	99	–4.38	8.3×10^{4}	2×10^{6}	94
Sample D (type III)	0.525	300	194	91	–3.85	2.7×10^{3}	2.9×10^{6}	18

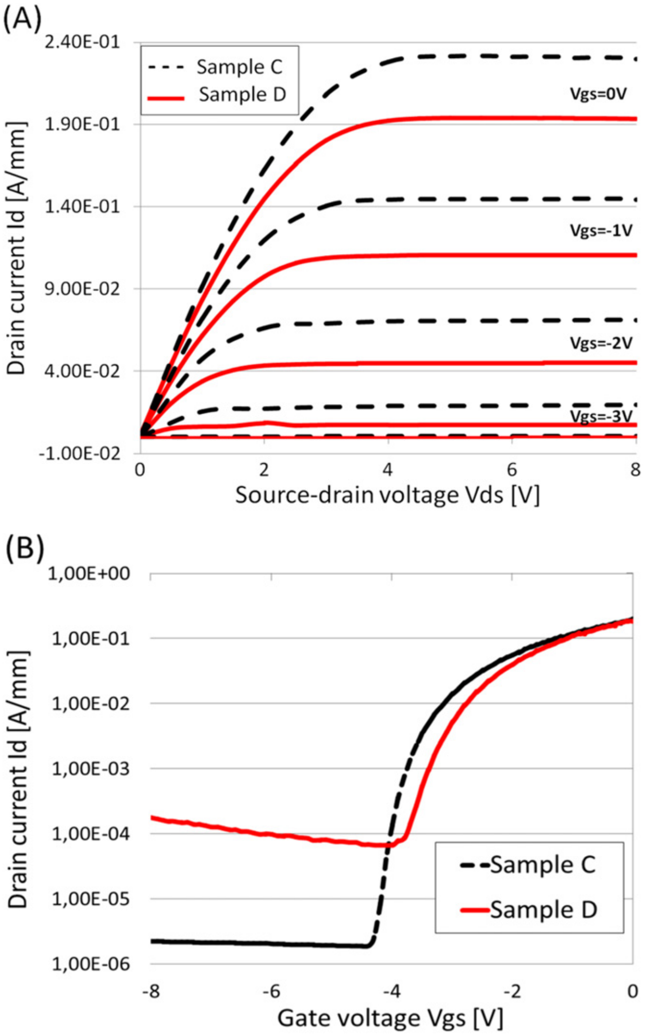

Figure 7. (A) Drain current as a function of drain-to-source bias of HEMTs on 300 nm GaN buffer with 200 nm AlN seed layer (continuous line) and 500 nm GaN buffer with AlN and AlGaN interlayer (dashed line). Drain voltage sweeps from 0 to 8 V while gate bias steps from 0 to −4 V with −1 V step. (B) Drain current as a function of the gate bias. Drain bias was set at 8 V, while gate bias varies from 0 V to −8 V with −0.1 V steps.

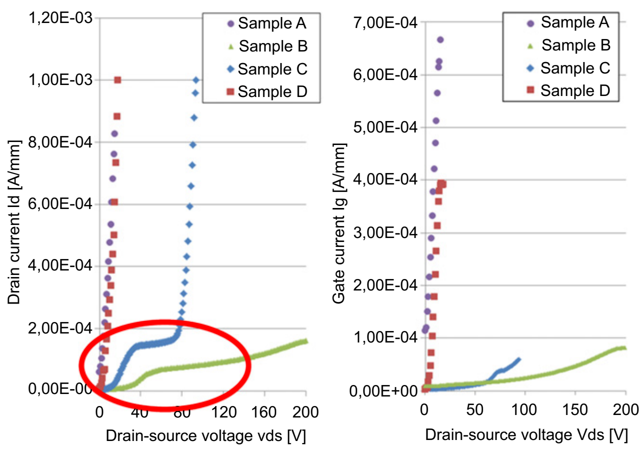

Figure 8. Drain leakage current (left) and gate leakage current (right) of AlGaN/GaN HEMTs with thin buffer. Compliance of 1 mA mm^{-1} was set for drain and gate current.

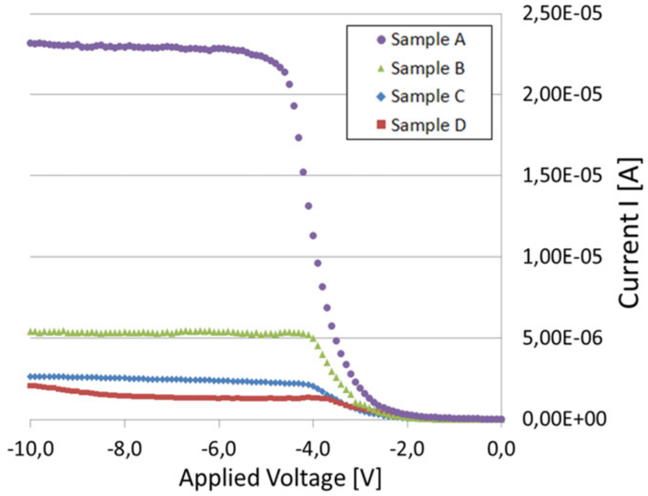

Figure 9. I–V measurements of 80 μm diameter circular schottky diode fabricated on samples A, B, C and D.

4. Summary

We have studied the evolution of material quality and electrical performances of AlGaN/GaN HEMTs grown on silicon with various buffer stacks and thicknesses. A 525 nm thick structure exhibits a carrier density and an electron mobility of 6.7×10^{12} cm^{-2} and 1147 cm^2 V^{-1} s^{-1}. HEMT device with normal DC output characteristics, saturated drain current of 194 mA mm^{-1}, an I_{on}/I_{off} drain current ratio of 2.7×10^3 and a Schottky diode reverse leakage current inferior to 0.06 A cm^{-2} have been achieved on this 525 nm structure. Even when the operation voltage required for the targeted NEMS application [29] is below the measured breakdown voltage, we notice a dramatic decrease of the latter while reducing the total thickness below 0.7 μm. With the view of integrating electronic function (amplifier) with the resonator while fulfilling mechanical and electrical NEMS requirements, further optimizations of the structures may be necessary. To do so, optimizations of the layer stacks, interfaces and growth conditions are currently investigated.

Acknowledgment

We acknowledge the support from the 'Investissements d'Avenir' GANEX (ANR-11-LABX-0014) and the ASTRID project AMGaSi funded by the French National Research Agency (ANR). Also, we thank Dr P Vennéguès for preparing the sample and taking the TEM image.

References

[1] Verd J, Uranga A, Abadal G, Teva J L, Torres F, López J, Perez-Murano F, Esteve J and Barniol N 2008 *IEEE Electron Device Lett.* **29** 146–8

[2] Bartsch S T, Lovera A, Grogg D and Ionescu A M 2012 *ACS Nano* **6** 256–64

[3] Ollier E, Dupre C, Arndt G, Arcamone J, Vizioz C, Duraffourg L, Sage E, Koumela A, Hentz S and Cibrario G 2012 *IEEE 25th Int. Conf. Micro Electro Mechanical Systems (MEMS)*
[4] Lopez J L, Verd J, Uranga A, Giner J, Murillo G, Torres F, Abadal G and Barniol N 2009 *IEEE Electron Device Lett.* **30** 718–20
[5] Nakao S, Ando T, Shikida M and Sato K 2006 *J. Micromech. Microeng.* **16** 715–20
[6] Mehregany M and Zorman C A 1999 *Thin Solid Films* **355** 518–24
[7] Sarro P M 2000 *Sensors Actuators* A **82** 210–8
[8] Adachi K, Watanabe N, Okamoto H, Yamaguchi H, Kimoto T and Suda J 2013 *Sensors Actuators* A **197** 122–5
[9] Cimalla V, Pezoldt J and Ambacher O 2007 *J. Phys. D: Appl. Phys.* **40** 6386–434
[10] Stutzmann M, Steinhoff G, Eickhoff M, Ambacher O, Nebel C E, Schalwig J, Neuberger R and Muller S 2002 *Diamond Relat. Mater.* **11** 886–91
[11] Li M, Tang H X and Roukes M L 2007 *Nature* **2** 114–20
[12] Masmanidis S C *et al* 2007 *Science* **317** 780
[13] Lin C-M, Chen Y-Y, Felmetsger V V, Senesky D G and Pisano A P 2012 *Adv. Mater.* **24** 2722–7
[14] Karabalin R B, Matheny M H, Feng X L, Defaÿ E, Le Rhun G, Marcoux C, Hentz S, Andreucci P and Roukes M L 2009 *Appl. Phys. Lett.* **95** 103111
[15] Kermany A R, Brawley G, Mishra N, Sheridan E, Bowen W P and Iacopi F 2014 *Appl. Phys. Lett.* **104** 081901
[16] Yonenaga I 2001 *Physica* B **308–310** 1150–2
[17] Gaska R, Chen Q, Yang J, Osinsky A, Khan M A and Shur M S 1997 *IEEE Electron Device Lett.* **18** 492–4
[18] Ivaldi P, Abergel J, Matheny M H, Villanueva L G, Karabalin R B, Roukes M L, Andreucci P, Hentz S and Defaÿ E 2011 *J. Micromech. Microeng.* **21** 085023
[19] Mastropaolo E, Cheung R, Henry A and Janzén E 2009 *J. Vacuum Sci. Technol.* B **27** 3109
[20] Uranga A, Teva J, Verd J, López J L, Torres F, Esteve J, Abadal G, Pérez-Murano F and Barniol N 2005 *Electron. Lett.* **41** 1327
[21] Maeda N, Tsubaki K, Saitoh T and Kobayashi N 2001 *Appl. Phys. Lett.* **79** 1634
[22] Maier D *et al* 2010 *IEEE Trans. Device Mater. Reliab.* **10** 427–36
[23] Mishra U K, Parikh P and Wu Y-F 2002 *Proc. IEEE* **90** 1022–31
[24] Herbecq N, Roch-Jeune I, Rolland N, Visalli D, Derluyn J, Degroote S, Germain M and Medjdoub F 2014 *Appl. Phys. Express* **7** 034103
[25] Palacios T, Chakraborty A, Rajan S, Poblenz C, Keller S, DenBaars S P, Speck J S and Mishra U K 2005 *IEEE Electron Device Lett.* **26** 781–3
[26] Ishida M, Ueda T, Tanaka T and Ueda D 2013 *IEEE Trans. Electron Devices* **60** 3053–9
[27] Gil B 1998 *Group III Nitride Semiconductor Compounds: Physics and Applications* (Oxford: Clarendon Press)
[28] Ansari A and Rais-Zadeh M 2014 *IEEE Trans. Electron Devices* **61** 1006–13
[29] Faucher M *et al* 2009 *Appl. Phys. Lett.* **94** 233506
[30] Popa L C and Weinstein D 2013 *The 17th Int. Conf. on Transducers & Eurosensors XXVI* pp 2461–4
[31] Vanko G, Hudek P, Zehetner J, Dzuba J, Choleva P, Kutiš V, Vallo M, Rýger I and Lalinský T 2013 *Microelectron. Eng.* **110** 260–4
[32] Amar A B *et al* 2012 *Appl. Phys. Express* **5** 067201
[33] Faucher M, Cordier Y, Semond F, Brandli V, Grimbert B, Amar A B, Werquin M, Boyaval C, Gaquière C and Théron D 2011 *IEEE 24th Int. Conf. on Micro Electro Mechanical Systems (MEMS)* 581–4
[34] Roukes M L 2000 *Technical Digest of the 2000 Solid-State Sensor and Actuator Workshop*
[35] Wang K, Wong A-C and Nguyen C-C 2000 *J. Microelectromech. Syst.* **9** 347–60
[36] Karabalin R B, Masmanidis S C and Roukes M L 2010 *Appl. Phys. Lett.* **97** 183101
[37] Chui B W, Stowe T D, Ju Y S, Goodson K E, Kenny T W, Mamin H J, Terris B D, Ried R P and Rugar D 1998 *J. Microelectromech. Syst.* **7** 69–78
[38] Rugar D, Budakian R, Mamin H J and Chui B W 2004 *Nature* **430** 329–32
[39] Yang Y T, Callegari C, Feng X L, Ekinci K L and Roukes M L 2006 *Nano Lett.* **6** 583–6
[40] Huang X M H, Feng X L, Zorman C A, Mehregany M and Roukes M L 2005 *New J. Phys.* **7** 247
[41] Senturia S D 2000 *Microsystem Design* (Boston, MA: Kluwer) pp 216–34
[42] Marti D, Tirelli S, Alt A R, Roberts J and Bolognesi C R 2012 *IEEE Electron Device Lett.* **33** 1372–4
[43] Rennesson S, Lecourt F, Defrance N, Chmielowska M, Chenot S, Lesecq M, Hoel V, Okada E, Cordier Y and De Jaeger J-C 2013 *IEEE Trans. Electron Devices* **60** 3105–11
[44] Medjdoub F, Zegaoui M, Grimbert B, Ducatteau D, Rolland N and Rolland P A 2012 *IEEE Electron Device Lett.* **33** 1168–70
[45] Cordier Y, Semond F, Lorenzini P, Grandjean N, Natali F, Damilano B, Massies J, Hoël V, Minko A and Vellas N 2003 *J. Cryst. Growth* **251** 811–5
[46] Lugani L, Carlin J-F, Py M A, Martin D, Rossi F, Salviati G, Herfurth P, Kohn E, Bläsing J, Krost A and Grandjean N 2013 *J. Appl. Phys.* **113** 214503
[47] Cordier Y, Pruvost F, Semond F, Massies J, Leroux M, Lorenzini P and Chaix C 2006 *Phys. Status Solidi* (c) **3** 2325–8
[48] Baron N *et al* 2009 *J. Appl. Phys.* **105** 033701
[49] Khoury M *et al* 2013 *Semicond. Sci. Technol.* **28** 035006
[50] Moram M A and Vickers M E 2009 *Rep. Prog. Phys.* **72** 036502
[51] Cordier Y *et al* 2007 *J. Cryst. Growth* **301–302** 434–6
[52] Hageman P R, Haffouz S, Kirilyuk V, Grzegorczyk A and Larsen P K 2001 *Physica Status Solidi and Applied Research* **188** 523–6
[53] Tang H, Baribeau J-M, Aers G C, Fraser J, Rolfe S and Bardwell J A 2011 *J. Cryst. Growth* **323** 413–7
[54] Zhang Y and Singh J 1999 *J. Appl. Phys.* **85** 587
[55] Wong Y-Y *et al* 2010 *J. Electrochem. Soc.* **157** H746
[56] Lecourt F, Douvry Y, Defrance N, Hoel V, Cordier Y and De Jaeger J C 2010 *Proc. of the 5th European Microwave Integrated Circuits Conf. (EuMIC) (Paris)* pp 33–6
[57] Cordier Y, Semond F, Massies J, Dessertene B, Cassette S, Surrugue M, Adam D and Delage S 2002 *Electron. Lett.* **38** 91–2
[58] Fleury C *et al* 2013 *Microelectron. Reliab.* **53** 1444–9
[59] Hsu J W P, Manfra M J, Molnar R J, Heying B and Speck J S 2002 *Appl. Phys. Lett.* **81** 79